

## MODELING OF HIGH-VELOCITY FLOWS IN ITAM IMPULSE FACILITIES

**Prof. A.M. Kharitonov**

Khristianovich Institute of Theoretical and Applied Mechanics SB RAS, Russia

It is well known that wind tunnels widely used at hypersonic velocities, are impulse and high-enthalpy facilities. These tunnels are based on different operation principles [1÷5, 14]:

|                                    |                  |
|------------------------------------|------------------|
| Blowdown wind tunnels              | several seconds; |
| Ludwieg tubes                      | up to 500 ms;    |
| Hotshot wind tunnels               | up to 150 ms;    |
| Adiabatic compression wind tunnels | up to 100 ms;    |
| Shock tubes                        | up to 10 ms;     |
| Shock tubes with a heavy piston    | up to 2 ms.      |

Because of the short test time in these facilities, it is necessary to estimate the times characterizing the duration of certain events  $\tau_{ev}$  in the flow around various models. In the flow around an oscillating body, for example,  $\tau_{ev}$  equals the oscillation period, and  $\tau_{ev} = \infty$  in the flow around a body moving with a constant velocity. If the model is rapidly inserted into the test section of the wind tunnel, it is important to determine the time of flow stabilization  $\tau_{stab}$ . Each wind tunnel (WT) also has its own characteristic time  $\tau_{WT}$  (time during which the stagnation parameters change by a certain factor). For instance, if the behavior of these parameters in the settling chamber is close to exponential,  $\tau_{WT}$  may be assumed to be equal to the time needed for the parameters to change by a factor of e. Interaction between the facility and the model is characterized by one more characteristic time. The model length being assumed to be  $L_{mod}$ , the fore and rear parts of the model experience the action of gas portions that leave the settling chamber at different times ( $\Delta t = \tau_{in} \sim L_{mod}/v_\infty$ , where  $v_\infty$  is the free-stream velocity in the test section); correspondingly, these gas portions have different stagnation conditions. Hence, the greater the value of  $\tau_{in}$ , the more non uniform is the flow around the model. Obviously, the relative non-uniformity is determined by the ratio  $\tau_{in}/\tau_{WT}$ . The lower this ratio, the more grounds are for neglecting it. The ratio  $\tau_{stab}/\tau_{WT}$  is subjected to similar requirements. If this ratio is small, this means that the flow pattern has enough time to follow the changing free-stream parameters.

Thus, the conditions  $\tau_{WT} \gg \tau_{in}$  and  $\tau_{WT} \gg \tau_{stab}$  should be always satisfied. Sometimes  $\tau_{in}$  and  $\tau_{stab}$  can coincide. For instance, in studying non-separated external flow past slender bodies,  $\tau_{stab}$  is approximately equal to the time of gas-particle flight along the model, i.e.,  $\tau_{stab} \approx L_{mod}/v_\infty \approx \tau_{in}$ . In the flow with boundary-layer separation, gas injection through the model surface, etc. However,  $\tau_{stab}$  is normally greater than  $\tau_{in}$ . If, in addition,  $\tau_{ev} \gg \tau_{stab}$ , the model can be assumed to be motionless (this is always valid if a steady flow is considered). In this case, the flow is assumed to be steady, the model is motionless, i.e., the flow parameters at infinity equal the instantaneous values at the nozzle exit. These features allow for experimental investigations of static aerodynamic characteristics with a continuous change of the angle of attack of the model during one run of the wind tunnel, if the model moves rather slowly (the time of model displacement is much greater than  $\tau_{stab}$ ). If the inequality  $\tau_{ev} \gg \tau_{stab}$  is violated, the phenomenon under study is essentially unsteady. For instance, acoustic waves obey the condition  $\lambda f = a$ , where  $\lambda$  is the wavelength,  $f$  is the frequency, and  $a$  is the

velocity of sound. In this case, obviously,  $\tau_{in} \approx \lambda/v_\infty$  or  $\tau_{in} \approx \frac{a}{fv_\infty}$ , and the inequality  $\tau_{in} \gg \tau_{WT}$  should be satisfied. Bearing in mind that,  $a/v_\infty \sim 1$  we obtain  $f \gg 1/\tau_{WT}$ . For  $\tau_{WT}=10\div20$  ms, the corresponding value should be  $f \gg 50\div100\Gamma_{II}$ . Hence, impulse facilities offer a reliable possibility of studying the behavior of turbulent oscillations, including acoustic oscillations with frequencies of about 1000 Hz and higher.

Another specific feature of impulse facilities is the quality of the flow, which includes the following basic characteristics:

- degree of spatial non-uniformity of parameters in the test section [1, 2];

The non-uniformity of the Mach number distribution should not exceed 1.5–2.0 %.

- size of the core flow, i.e., the region with uniform parameters;

The core flow diameter is estimated as 50 – 70% of the nozzle exit diameter.

- purity of the flow, i.e., degree of contamination of the test gas by foreign particles (products of electrode erosion, etc.).

Contamination of the air flow by active radicals generated by dissociation and ionization of air components at stagnation temperatures higher than  $\sim 3000$  K.

Usually the flow quality is found by both direct measurements of uniformity of parameters in the core flow, size of the core flow, and degree of flow contamination, and by indirect methods by testing reference models and comparisons with similar data obtained in other wind tunnels.

Several impulse wind tunnels are in operation at ITAM SB RAS: IT-302 wind tunnel with a discharge chamber, AT-303 wind tunnel with adiabatic compression, and shock tubes. Basic and applied aerodynamic research has been performed in these wind tunnels in the range of Mach numbers  $M = 6 \div 20$  for many years.

## **1. Hot-shot wind tunnel with a discharge chamber IT-302**

It is well known that the main feature of impulse facilities with a discharge chamber is test-gas exhaustion from a closed volume and, hence, continuously decreasing pressure, density, and temperature during the test regime. In this case, a question arises on an admissible degree of quasi-steadiness of the flow. This means that it is necessary to estimate the relative rate of pressure variation in the test section or the degree of quasi-steadiness  $K = |(dp/dt)p|$  in the test regime, which is inversely proportional to the volume of the settling chamber and directly proportional to the nozzle-throat area. Calculations [3] performed for different types of tests show that the degree of quasi-steadiness  $K \leq 50 s^{-1}$  (or 5% during 1ms) does not induce any noticeable distortions in the flow around the models.

Distinctive features of wind tunnels with a discharge chamber are simplicity of their structure and compactness. In contrast to classical wind tunnels, the settling chamber of hot-shot tunnels is first filled by the test gas with a pressure of 100–200 atm, which is then heated by a pulsed arc discharge. At the beginning, the settling chamber is separated from the test section by a diaphragm mounted in the subsonic part of the nozzle, while the gas from the remaining part of the wind tunnel (nozzle, test section, and vacuum tank) is evacuated by vacuum pumps to a pressure of  $\sim 10^{-2}$  mmHg. During the discharge of the capacitor  $C_{cap}$  (the discharge duration is  $\sim 0.4\text{--}1.5$  ms) or inductive accumulator ( $10\div20$  ms), the temperature and pressure of the test gas drastically increase. When the required pressure is reached, the

diaphragm breaks down, and the gas starts exhausting through the nozzle into the test section. After a short transitional process ( $\sim 1$  ms), a flow with a prescribed Mach number is generated. The test time in hotshot wind tunnels depends on the settling chamber volume and normally reaches 50–150 ms.

Thus, each run of the hot-shot wind tunnel includes four steps: 1 – heating of the test gas by an arc discharge, 2 – reaching a required test regime, 3 – test regime proper, 4 – breakdown of the test regime.

Several tenths of a millisecond after the discharge, the diaphragm separating the settling chamber from the remaining part of the wind tunnel is opened and non-stationary exhaustion of the gas from the settling chamber begins. This flow is accompanied by a system of gas-dynamic discontinuities moving along the nozzle and passing through the test section where the model is mounted. The moment when the “last” discontinuity passes through the test section determines the WT start-up time. This time is characterized by passage of a shock wave propagating over a cold rarefied gas filling the wind tunnel. When the gas heated in the shock wave (plug) passes around the model, there appears a contact surface with intense mixing of the gas. All this time reaches  $\sim 1.5$  ms. The test time in such wind tunnels, i.e., the time of the quasi-steady flow around the model, is usually 50–150 ms. As the Mach number decreases, the test time rapidly decreases because of an increase in the nozzle-throat area and, correspondingly, flow rate of the gas. The thermodynamic parameters of the flow (pressure, density, and temperature) and, correspondingly, the Reynolds numbers become lower. At the same time, the Mach number remains almost unchanged.

The hot-shot wind tunnel with a discharge chamber consists of the following basic elements: high-pressure chamber, electric-arc discharge system, settling chamber, nozzle, test section with an Eiffel chamber, and exhaust system with a vacuum tank.

The main drawback of such type wind tunnels for example like F4 related to a continuous decrease in  $P_0$ ,  $\rho$  and  $Re$  during the test time. But the using pressure multipliers ensure constant stagnation parameters during WT operation. Such hot shot wind tunnel IT-302 (Fig. 1) was commissioned at ITAM SB RAS and successfully operates since 1985 [4, 5].

This wind tunnel differs from other available hot-shot wind tunnels because it has a pressure multiplier 5, which maintains constant flow parameters. The pressure multiplier is a two-step piston 6 set into motion at the moment the diaphragms 3 and 11 are broken, which moves in the discharge chamber under the control of a special controller 9. The piston compresses the exhausting gas, thus, maintaining a constant stagnation pressure during the

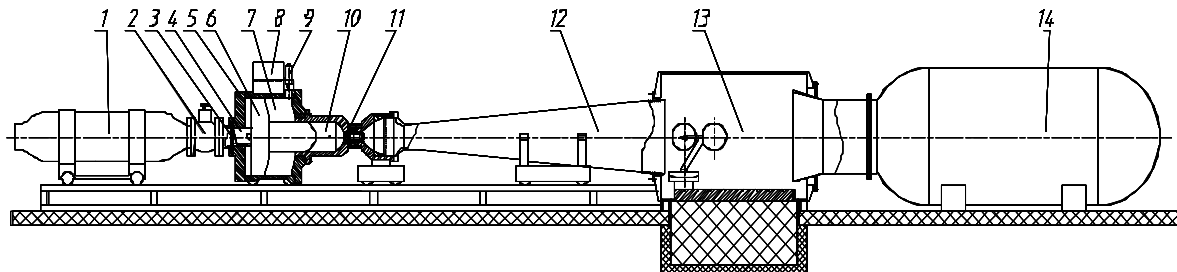


Fig. 1 Sketch of the IT-302 hot-shot wind tunnel with a pressure multiplier: 1 – gas holder (4100 liters with a pressure  $P_{\max} = 200$  atm); 2 – shutoff valve; 3 – diaphragm 3; 4 – plunger; 5 – pressure multiplier; 6 – two-step piston; 7 – damping fluid; 8 – tank for fluid; 9 – controller of the flow rate; 10 – discharge chamber; 11 – diaphragm 3; 12 – contoured nozzle; 13 – test section; 14 – vacuum tank

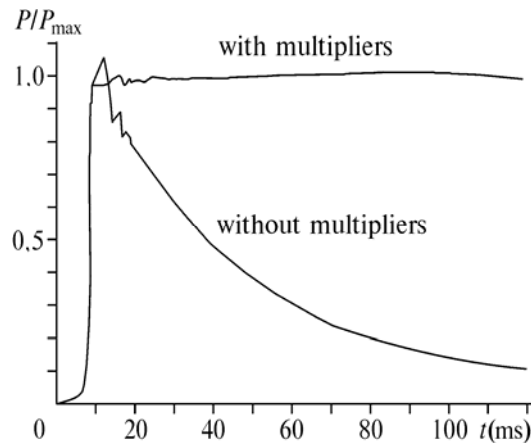


Fig. 2 Pressure oscillogram in the settling chamber with and without the pressure multiplier.

those with combustion of various fuels, characteristics of models of reentry vehicles, various methods of thermal protection, properties of a hypersonic boundary layer, and interaction of the latter with shock waves.

The thrust-aerodynamic characteristics of a model scramjet with a three-dimensional inlet [6, 7, 8] with horizontal and side compression wedges (Fig. 3) were experimentally studied. The modular structure of the model allowed testing both the complete configuration of the engine and the isolated inlet.

The scramjet model was tested in the IT-302 hot-shot wind tunnel in regimes without combustion and with combustion of gaseous hydrogen. External compression of the inlet is ensured by the main wedge with an angle  $\theta_{\text{hor}} = 12.5^\circ$  and a swept leading edge located horizontally, as well as by two side wedges with angles  $\theta_{\text{side}} = 10^\circ$  and sweep angle  $\chi_{\text{side}} = 45^\circ$ . The choice of the parameters of the internal compression section of the inlet was determined, first, by conditions of model testing with combustion in IT-302 within the Mach number range  $M_\infty = 4 \div 8$  and, second, by the desire to obtain good performance of the model with a fixed inlet geometry in blowdown wind tunnel T-313 at  $M = 4$  and 6 in regimes without fuel injection.

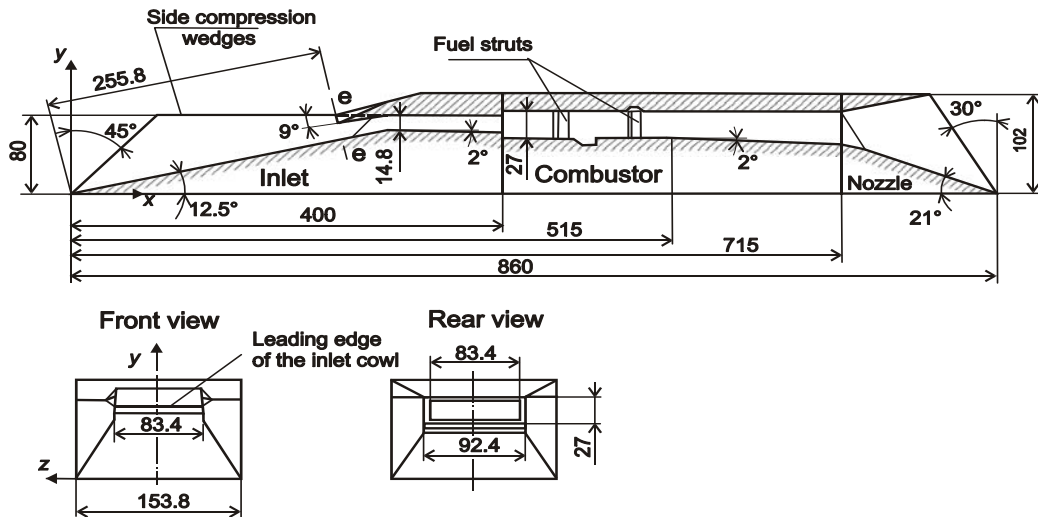


Fig. 3 General Layout of the model engine.

test time until the test regime is terminated. A typical oscillogram of pressure in the settling chamber, obtained with the pressure multiplier, is shown in Fig. 2. The pressure remains constant during about 0.1 s within  $\pm 1\%$ . For comparison, the figure also shows the pressure oscillogram for the case of WT operation without the pressure multiplier.

The Mach number in the test section remains practically constant, because it is mainly determined by the ratio of nozzle-exit and nozzle-throat areas.

This unique WT is used up to now to study various problems of gas dynamics: specific features of compression and expansion flows in inlets and model scramjets, including

The inner duct of the inlet has a rectangular cross section and is finished by a downward-facing step with abrupt expansion of the cross-sectional area to a value corresponding to the initial cross section of the combustion chamber  $A_{\text{comb}}/A_0 = 0.2$ . The combustor has an initial sector with a constant cross-sectional area, where two rows of vertical struts for injection of gaseous hydrogen were mounted. The nozzle formed by flat walls in the simplest manner as an “inverse” inlet ensures expansion of the exhausted jet in the horizontal and vertical planes. The exit section of the nozzle is made oblique with an angle  $\chi_n = 30^\circ$  and has a relative area  $A_n/A_0 = 1.275$ .

During the experiments, the schlieren pictures of the flow pattern in the duct were obtained; detailed measurements of static pressure and heat flux distributions on compression wedges of the inlet and in the scramjet duct and stagnation pressure distributions in the exit cross section were performed by means of Pitot rakes.

The axial component of the resulting forces acting on the model was measured by a special external strain-gauge balance located on the sting under a protective shield. The system of fuel injection into the model did not affect the balance measurements. The drag of the main components of the scramjet was determined, and the resulting thrust-aerodynamic characteristics of the examined model configuration of the scramjet were obtained.

As a whole, the flow pattern in the inlet is characterized by complicated multiple three-dimensional interactions of shock waves with each other and with the boundary layer. Glancing shock waves induce numerous three-dimensional separations and reattachments. The system of shock and expansion waves formed in the inlet is responsible for significant non-uniformity of the velocity field at the combustor entrance.

In model testing with combustion with  $M_\infty = 8$ , the pressure in the fuel tank was maintained constant, and the air-to-fuel ratio was  $\alpha = 0.7–1.2$ . Figure 4 shows an example of static pressure and heat flux distributions along the model for  $M_\infty = 8$  at the time about  $\tau = 120$  ms. The pressure is normalized to the free-stream value, and the heat flux is normalized to the flux of specific kinetic energy  $C_q = q_w / (\rho_\infty V_\infty \cdot V_\infty^2 / 2)$ . Here  $\rho_\infty$ ,  $V_\infty$ , and  $q_w$

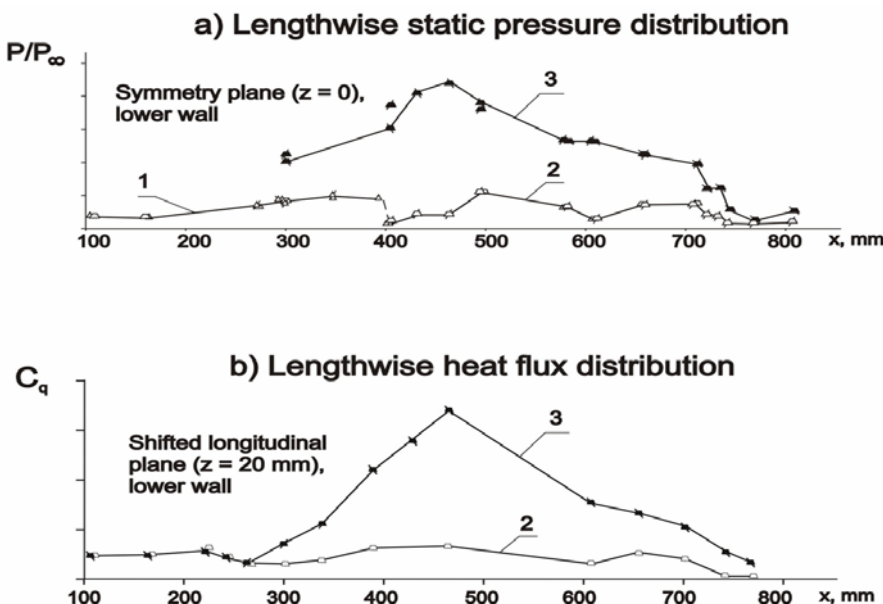


Fig. 4 Distributions of pressure (a) and heat fluxes (b) along the model: 1) inlet; 2) regime without fuel injection; 3) regime with combustion of gaseous hydrogen

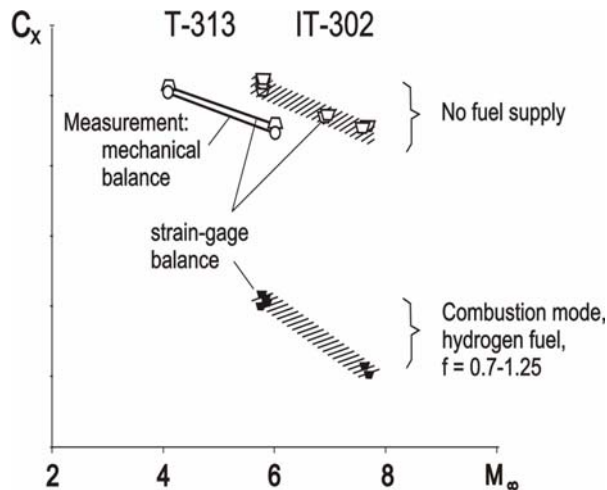


Fig. 5 Coefficient of the longitudinal force of the model

and a pseudoshock in the model inlet was also observed for  $M_\infty = 6$  in the time interval  $\tau = 80 - 120$  ms.

The characteristics of the longitudinal thrust-aerodynamic force obtained in testing the complete scramjet model in regimes with and without hydrogen combustion are shown in Fig. 5 as the coefficient of the longitudinal force of the model  $C_x = X/(q A_0)$  versus the Mach number. Here  $X$  is the axial component of the resulting forces acting on the model in the longitudinal direction and  $q_\infty$  is the dynamic pressure. In T-313 tests, the aerodynamic forces measured by the mechanical and strain-gauge balances are in reasonable agreement. For the complete model, the disagreement is smaller than 4%. In IT-302, the tests were performed in small series, where good agreement of balance measurements was obtained with a scatter within 4%. It is worth noting that the character of variation of the longitudinal force coefficient of the model as a function of the Mach number is identical in both wind tunnels in regimes without fuel injection, which is evidenced by an almost identical slope of the "curves"  $C_x(M_\infty)$  for  $M_\infty = 4-6$  in T-313 and for  $M_\infty = 6-8$  in IT-302. The axial drag force acting in the downstream direction significantly decreases in regimes with hydrogen combustion, i.e., internal thrust of the engine is obtained. A decrease in drag of the model scramjet due to internal thrust was approximately 58% for  $M_\infty = 6$  and 67% for  $M_\infty = 8$ .

Some difference in  $C_x$  is caused by the lower free-stream Mach numbers  $M_\infty = 5.6-5.8$  in IT-302 as compared to  $M_\infty = 6$  in T-313 and also can be explained by the difference in flow parameters in the experiments. IT-302 has significantly lower Reynolds numbers per meter as compared to T-313. Thus, comparative tests of the model at  $M_\infty = 6$  were performed with  $Re_1 = 18-20 \times 10^6$  in T-313 and with  $Re_1 = 2-2.5 \times 10^6$  in IT-302.

The same model was tested in the new wind tunnel AT-303 with combustion of gaseous hydrogen [9].

The pressure distribution along the scramjet model in regimes without fuel injection and with combustion of gaseous hydrogen confirmed the existence of a thermal pseudoshock regime of combustion considered previously [9, 10].

The model scramjet and the model with a convergent inlet were investigated within the framework of ITAM cooperation with Dassault Aviation.

are the free-stream density and velocity and the specific heat flux, respectively. The level and behavior of pressure and heat fluxes along the scramjet duct show that a flow regime with thermal choking in the model inlet is obtained.

A flow regime with a system of  $X$ -shaped oblique and glancing shock waves is formed, which can be interpreted as a pseudoshock [9, 10]. The beginning of pressure increase in the pseudoshock is established at the entrance section of the inlet ahead of the throat by the time  $\tau = 80$  ms, but apparently, the pseudoshock does not go upstream of the inlet duct. The quasi-steady flow regime with thermal choking in the combustor

observed for  $M_\infty = 6$  in the time interval  $\tau = 80 - 120$  ms.

## 2. Original wind tunnel with adiabatic compression AT-303

The adiabatic compression wind tunnels do not give such high stagnation temperatures as hot-shot and shock tunnels, but, owing to higher densities and pressures, they ensure high Reynolds numbers. One of the first tunnels based on this principle is the Long-Shot facility [5, 11] at the Von Karman Institute (Belgium). It is designed for operation with nitrogen with initial pressures up to 4000 atm and temperatures up to 3000 K.

High pressures can be obtained by using gas sources with a completely adiabatic cycle of test-gas preparation. Such sources are equipped with pressure multipliers consecutively compressing and then ejecting the gas at constant pressure. The first source of the test gas of this kind was created at the Lavrentyev Institute of Hydrodynamics of the Siberian Branch of the Russian Academy of Sciences (LIH SB RAS) in 1975 [12, 13, 14].

One of the main problems of wind tunnels with adiabatic compression and a free piston is piston kickback after its stop at the point of the maximum compression. At the maximum pressures of the test gas of the order of 2000÷4000 atm, almost the entire process of piston deceleration occurs during the last tens of microseconds (increase in pressure from the halved to the maximum value) [13]. The piston kickback and the decrease in pressure occur during the same time period; hence, it is necessary to lock the gas in the settling chamber or to stop the piston at the point of the maximum compression. Both processes are rather difficult tasks in the technical aspect. In the first case, it is necessary to ensure a large cross-sectional area, fast response, and erosion resistance of check valves, which are contradictory requirements. In the second case, it is necessary to resolve the issue of a very large force acting on the channel, because the force acting on each square centimeter of the piston area is 2 ÷ 4 tons.

For example in the Long-Shot wind tunnel with adiabatic compression [5], the settling chamber is equipped with a system of 48 valves preventing the gas backflow into the channel. At the final stage of compression, the gas with very high parameters penetrates through the valves, leading to their erosion and rapid failure. It is probably for this reason that Long-Shot operates with nitrogen only. In the wind tunnel with adiabatic compression, which was developed at SB RAS, the piston is equipped with a special system of wedges, which terminate the piston motion without kickback at the point of the maximum pressure, its seizure, and free motion after the pressure in the settling chamber is released [14]. As a result, heat losses and gas contamination become lower.

The concept and experience of exploitation of the model facility developed at LIH SB RAS were used to develop a new wind tunnel with adiabatic compression (AT-303) at ITAM SB RAS [5, 14]. A sketch of the wind tunnel is shown in Fig. 6. The main element of this wind tunnel is the source of high-pressure gas with a volume of the settling chamber approximately equal to 6 dm<sup>3</sup>, which was developed in the 1980s by LIH SB RAS [12, 13]. This source allows obtaining pressures up to 3000 atm and temperatures up to 2000 K. The test time is 40÷100 ms, and the nozzle-exit diameters are 0.3-0.6 m. The test gases are nitrogen, air, helium, or CO<sub>2</sub>. It is a completely symmetric system with two pressure multipliers, which are set into motion by eight pneumohydraulic drives. The main pressure multipliers are fed by a cross scheme providing rigorous hydraulic synchronization of the opposing motion of the pistons. The gas is injected into the settling chamber through a Cowper-type heater at a pressure of 170 atm and temperature of 900 K; then it is compressed by the pressure multipliers to prescribed parameters and is ejected through the nozzle.

At the start-up moment, the gas with a pressure up to 300 atm from receivers enters the pneumohydraulic drives. The pressure of the fluid increases to 1500 atm, affecting the main pressure multipliers, which start moving toward each other and adiabatically compress the test

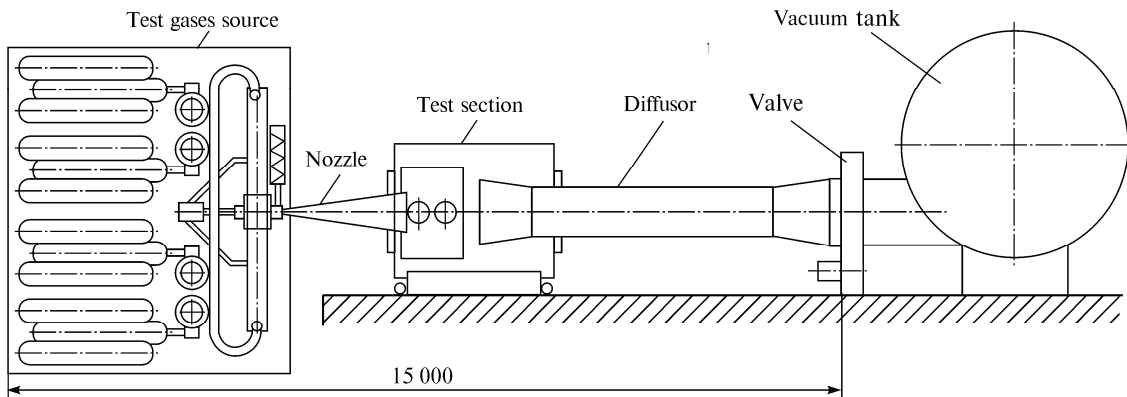


Fig. 6. Sketch of the AT-303 wind tunnel with adiabatic compression at ITAM SB RAS.

gas to prescribed parameters. When a necessary pressure in the settling chamber is reached, a special valve opens the nozzle throat during  $\sim$  ms, and gas exhaustion begins.

The remaining elements of AT-303 are typical of hypersonic wind tunnels (see Fig. 6): nozzle, test section, output diffuser, and vacuum tank with a volume of  $250 \text{ m}^3$ . The wind tunnel is fed from an in-house compressor station, which provides pressures up to 350 atm and a total volume of gas holders of  $4 \text{ m}^3$ . By virtue of adiabatic of the test-gas preparation cycle, the process of gas compression has an isentropic character. Hence, the parameters

reachable in the settling chamber are rigorously related to the initial parameters. If the initial parameters are defined, the possible states of the gas lie on one isentropic in the plane  $P_0 - T_0$ .

In the M-Lg( $Re_D$ ) coordinates, Fig. 7 shows the theoretically calculated Mach and Reynolds numbers that can be reproduced in AT-303. The data are plotted on the background of a region bounded on the bottom by the trajectory of reentry vehicles, such as Buran or Shuttle, and bounded on the top by a conventional trajectory of an aerospace plane with a dynamic pressure of 75 kPa. The solid curves show the logarithms of the maximum reachable Reynolds numbers versus the Mach number on the line of equilibrium condensation of air for nozzle-exit diameters  $D = 300 \text{ mm}$  (Mach numbers 8÷20) and  $600 \text{ mm}$

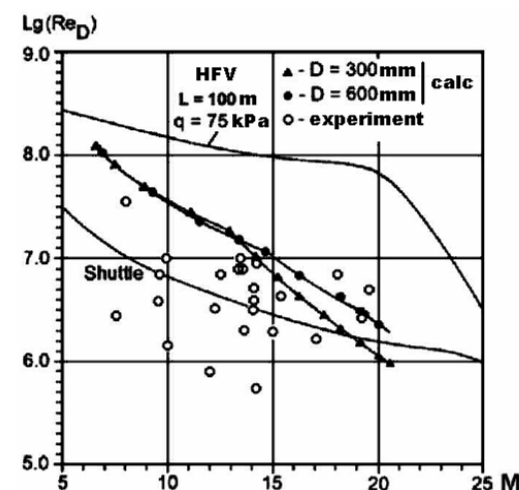


Fig. 7

( $M = 14 \div 20$ ). The Reynolds numbers  $Re_D$  are calculated on the basis of these diameters.

For the maximum pressure in the settling chamber (3000 atm), the stagnation pressure of the flow is 400 atm.

The open symbols indicate test regimes with measurements of non-uniformity of the fields of flow parameters in the test section. As is seen from Fig. 7, AT-303 reproduces natural values of the Mach and Reynolds numbers for testing large-scale models of promising aerospace planes with hypersonic scramjets.

Thus, the use of high pressures and moderate temperatures in hypersonic wind tunnels with adiabatic compression equipped by pressure multipliers allows reproduction of natural conditions in terms of the Mach and Reynolds numbers with test times of  $\geq 40$  ms. In addition

to high purity of the test gas, the wind tunnel makes it possible to test models of hypersonic flying vehicles with inlets, combustors (with combustion), and nozzles.

Another advantage of facilities of this type is the possibility of separating the influence of viscosity and real gas effects in studying the flow around models of hypersonic flying vehicles. This is particularly important for verification of CFD models and methods under development.

Some examples of the hypersonic flows around different models are given below.

**Hyperboloid flare (HF) model** [16] whose profile describes the windward centerline of the Hermes re-entry vehicle at an angle of attack. The contour is defined by ESA/ESTEC, Schwane and Muylaert (1994), as matched fourth order polynomials for the axial coordinate  $X$  as a function of the surface abscissa  $Y$ , including a flare making an angle of 43.60 with  $X$ -axis. The model was instrumented with 20 Kulite pressure transducers, type XCS-093-50D. Seventeen transducers were located along one generatrix of the model. The model was also instrumented with 17 ONERA thermocouples.

Figure 8 show the schlieren pictures of the flow around the HF models with small and big flare at the Mach number equal to 10.

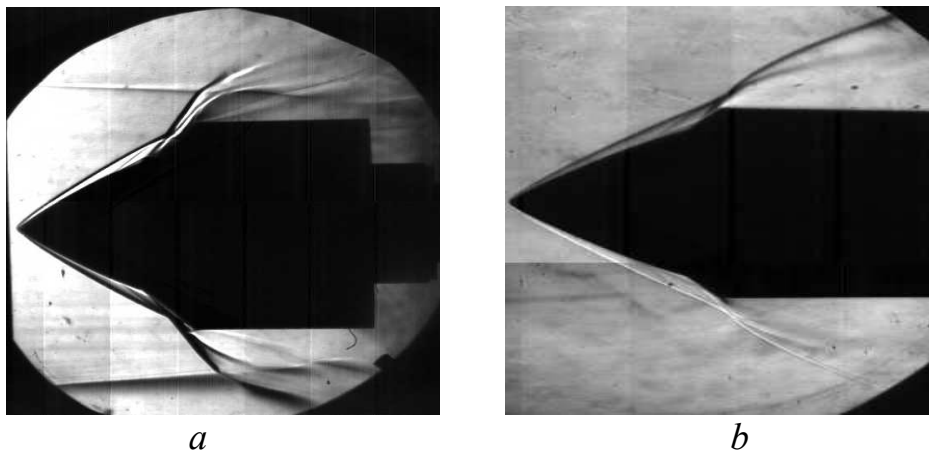


Fig. 8 Big flare at  $M = 9.94$ ;  $Re_L = 2.8 \times 10^6$  (a); small flare at  $M = 9.91$ ;  $Re_L = 2.62 \times 10^6$  (b).

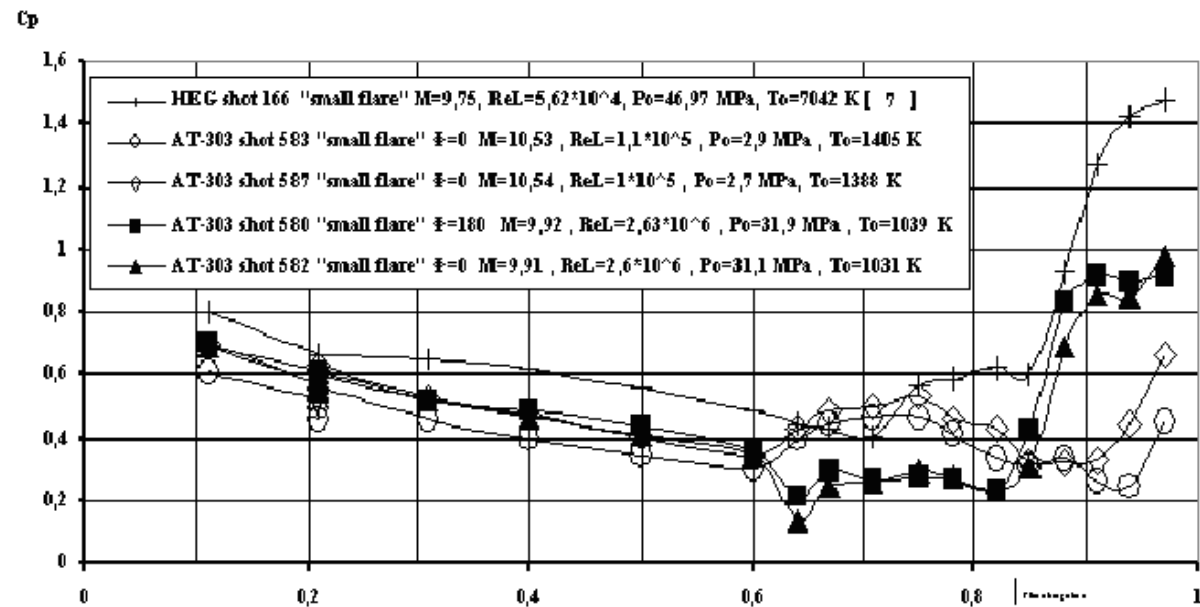


Fig. 9 Comparisons of the pressure coefficient distributions

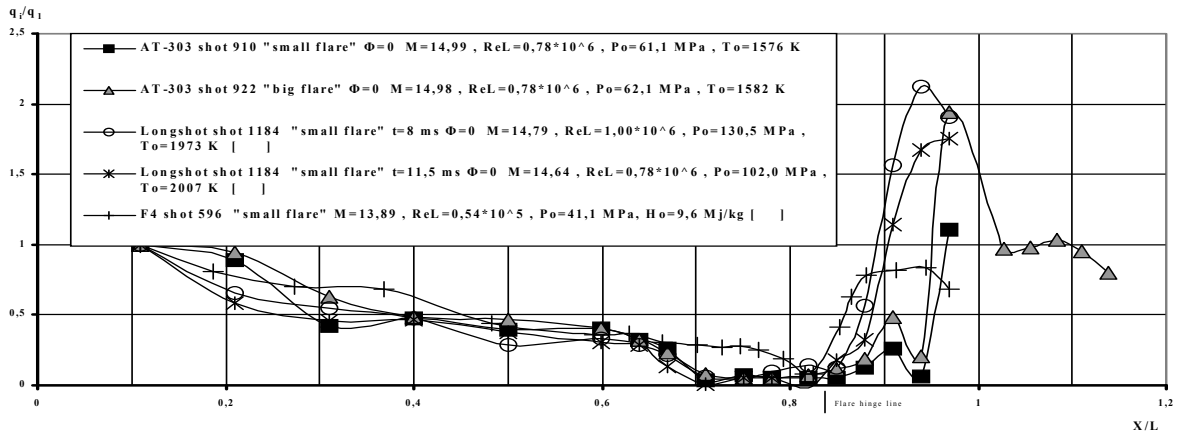


Fig. 10 Distributions of the relative heat fluxes

The pressure coefficients measured in AT-303 at  $M_\infty = 10$  (Fig. 9) are compared with similar data obtained in the HEG high-enthalpy wind tunnel, where the maximum Reynolds number is  $Re_L \approx 5.6 \times 10^4$ , which is approximately 2 times lower than the minimum value of  $Re_L$  in AT-303 and 46 times lower than the maximum value.

The distributions of the relative heat fluxes (Fig. 10) measured in AT-303, Long-shot, and F-4 are compared. Up to the beginning of the flare, all data are in good agreement within the measurement accuracy and difference in flow parameters. The greatest differences are observed in the vicinity of reattachment of the separated boundary layer, which is, apparently, related to the influence of  $Re_L$  and unsteadiness. This is evidenced by the results observed using a CCD camera with a filming frequency of 1000 frames per second.

Analyzing the results of comparisons of the pressure distributions obtained in the AT-303 and HEG wind tunnels, one should remember that AT-303 ensures modeling of viscous effects only, whereas HEG models real gas effects to a certain extent and does not model viscous effects.

The distributions of the relative heat fluxes obtained in AT-303 and HEG for  $M \approx 10$  are compared. A significant effect of  $Re_L$  on the heat-flux distribution in the vicinity of the reattachment boundary layer on the model with the short flare is observed. Note that the distribution of the relative heat fluxes obtained in HEG at  $T_0 \approx 7042\text{K}$  (nonequilibrium gas) is close to data obtained in AT-303 at low  $Re_L$ . The heat fluxes measured in AT-303 at  $M \approx 10$  for  $Re_L$  numbers that differ by more than an order of magnitude are shown here. The maximum heat flux occurs in the reattachment region, exceeding the corresponding level at a lower Reynolds number by an order of magnitude. This is an example, which shows some frames of the schlieren pictures of the flow around the HF models with long a) and short b) flares. It is worth noting that the interaction of the bow shock wave with separated shocks occurs in the vicinity of the corner point in case a) and near the flare surface in case b), which leads to redistribution of surface pressures and heat fluxes.

Thus, the previous conclusions on advantages of AT-303 for adequate modeling of the thermal characteristics of re-entry vehicles in a wide range of governing parameters are supported.

**Aerodynamic characteristics of the ARES.** The Aerospace Demonstrator ARES geometry (Fig. 11) was proposed by EADS-ST, and its tests in AT-303 at natural Reynolds numbers (Fig. 12) were performed within the framework of the ISTC project Nos. 2109 and 3550 with direct participation of Dr. Jean-Claude Paulat [17, 18]. The ARES model was

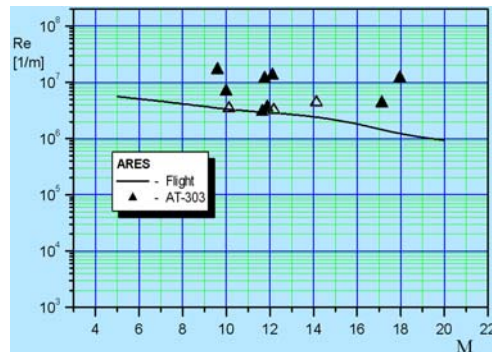


Fig. 11



Fig. 12

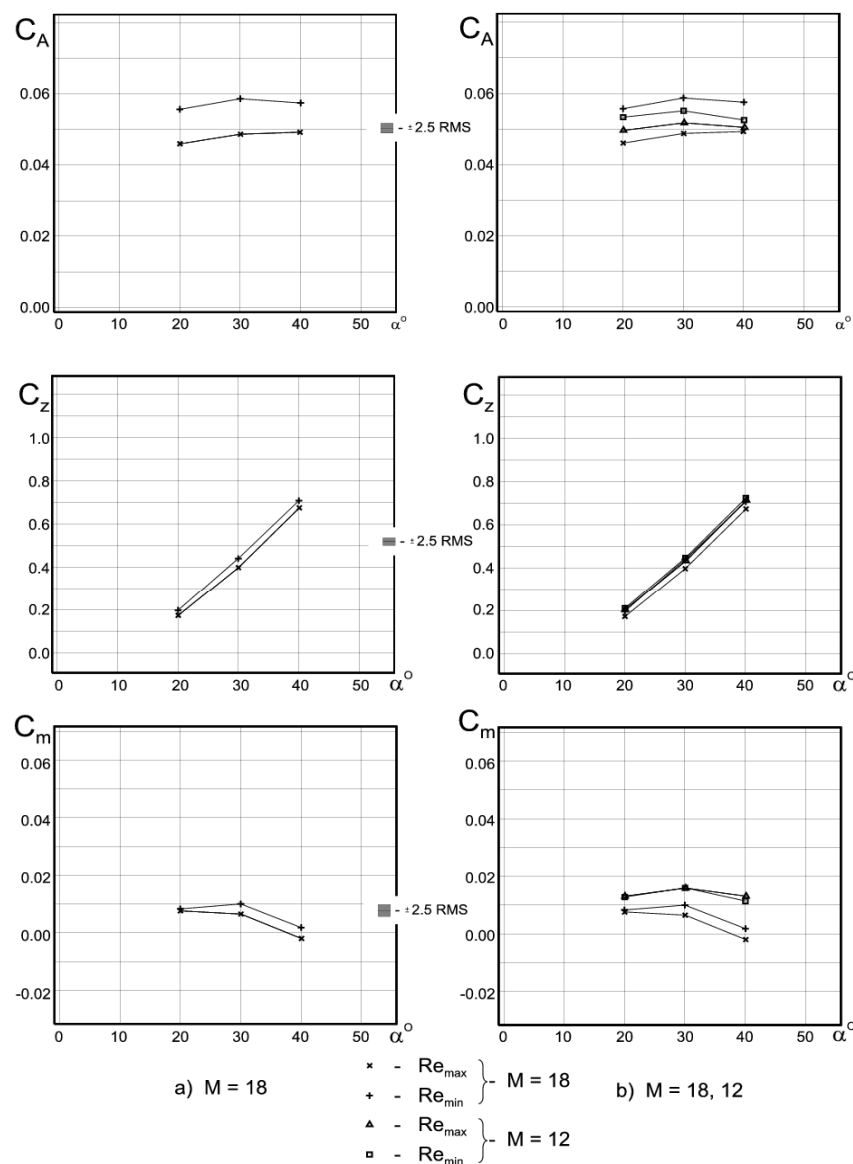


Fig. 13 Aerodynamic characteristics for  $M_{\infty} = 12$  and  $18$  obtained in a conical nozzle

tested on some parts of the reentry trajectory at nominal Mach numbers  $M = 10, 12, \text{ and } 18$  at angles of attack  $\alpha = 20^\circ, 30^\circ, \text{ and } 40^\circ$ . The aerodynamic characteristics of the ARES model with allowance for corrections for flow conicity are shown in Fig. 13. The results obtained characterize the drag, lift, and pitching moment coefficients as functions of the angle of attack and Reynolds number. A comparison of the moment characteristics shows that the pitching moment decreases with increasing  $M$  (the center of pressure is shifted backward), the static stability increases, and the balancing angle of attack decreases to  $\alpha \approx 40^\circ$ . The influence of the Reynolds number on these data is within the measurement error. These are approximate estimates of their real values under conditions of a parallel flow and can be used in practice only in this aspect. To obtain more reliable values of aerodynamic characteristics, it is necessary to perform tests with a contoured nozzle or determine more justified corrections for flow conicity.

**Aerodynamic characteristics of the EXPERT reentry Capsule.** The concept and geometry of this capsule were proposed by ESA ESTEC [19, 20]. The general view of the model (scaled 1:8) and required values of the Reynolds numbers are shown in Fig. 14. A large series of balance tests was performed at Mach numbers  $M = 10, 12, 14, \text{ and } 18$ , angles of attack  $\alpha = 0^\circ, 3^\circ, \text{ and } 6^\circ$ , and natural Reynolds numbers. The flow around this model, even at a zero angle of attack, is rather complicated and is accompanied by separated flows in the vicinity of the flaps with propagation of vortices in the gaps between the flaps. It can be assumed that flow reconstruction with some periodicity in time occurs under these conditions.

Force measurements in the AT-303 facility were carried out with the help of a six component strain-gage balance. Multiple tests at  $M = 10$ ,  $Re \sim 6-7 \cdot 10^6 \text{ 1/m}$ , and  $\alpha = 6^\circ$  were performed, aimed at determining the mean-square deviations of measured data directly for the EXPERT model. As a result, the following values of mean-square deviations were obtained:

- for longitudinal force  $\sigma_{C_A} = 0.0041$ ;
- for normal force  $\sigma_{C_Z} = 0.0024$ ;
- and pitch moment  $\sigma_{m_z} = 0.0022$ .

Thus, the measured values of aerodynamic coefficients include random errors equal to  $\pm 2\sigma$ , which corresponds to a confidence probability of  $P \sim 0.95$  in the Student distribution.

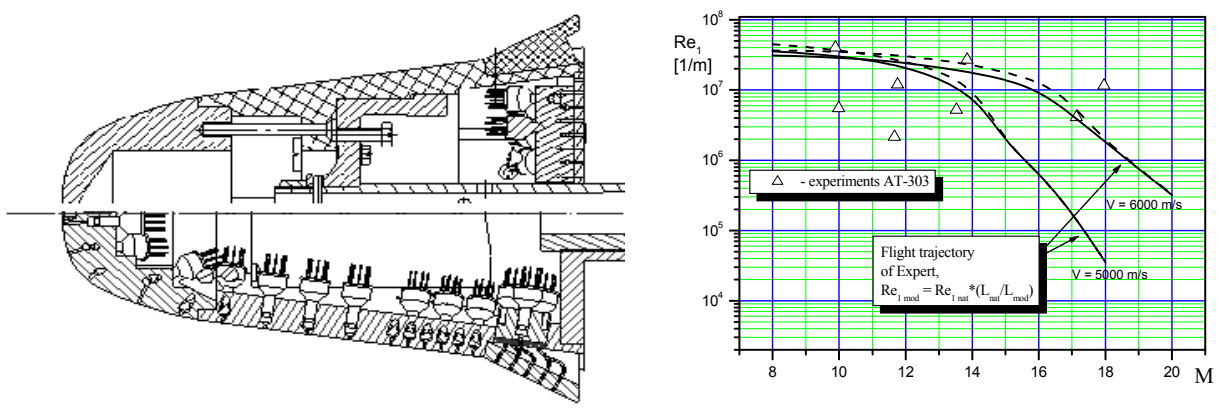


Fig. 14. Longitudinal section of the EXPERT model with heat-flux probes, 20 pressure gages on the opposite generatrix and 22 pressure gages on the base surface (a) and required values of the Reynolds number per meter (b).

This errors were then used to analyze the test data obtained at  $M = 14$  and  $18$ .

#### Total aerodynamic characteristics.

The experimental data obtained are shown in Fig. 15 for aerodynamic-force coefficients in the balance-fitted coordinate system. The same figure shows the probable level of random errors as predicted from previous data obtained in multiple tests at  $M = 10$  [21, 22].

It should be noted that the longitudinal force coefficient, varying in the interval  $C_A \sim 0.310\text{--}0.335$ , displays an insignificant (within 10%) increase over the angle of attack. Repeated tests at  $\alpha = 6^\circ$  show rather good convergence of data, especially for the longitudinal force coefficient  $C_A$ . The scatter in the measured values of the normal force and pitching moment coefficients lies within the limits of the square-mean deviation.

The effect of the rolling angle generated by model rotation with respect to the longitudinal axis of the balance was investigated at  $\alpha = 6^\circ$ . The data were obtained for rolling angles  $\gamma = 0, 45$ , and  $90^\circ$ . Recall that the angle  $\gamma = 0$  refers to the open state of one of the flap pairs in the vertical symmetry plane, and the angle  $\gamma = 90^\circ$ , in the horizontal symmetry plane. The scatter of  $C_A$  can be argued to be within  $\pm 2\sigma_{C_A}$ . The normal force and pitching moment coefficients display a similar behavior, although the scatter of experimental values here is more pronounced.

**Pressure distribution over the model surface.** The pressure distributions over the surface of the EXPERT model were measured at the Mach number  $M = 10$  (conical nozzle with the exit diameter  $D_n = 400$  mm) at the following values of free-stream parameters: stagnation pressure  $P_0 = 9850$  kPa, stagnation temperature  $T_0 = 1024$  K, and unit Reynolds number  $Re_1 = 6.8 \cdot 10^6$  1/m. The obtained pattern of the relative pressure over the generatrix of the windward and leeward surfaces in the plane of symmetry of the model is shown in Fig. 16 for the angles of attack  $\alpha = 0, 3$ , and  $6^\circ$  [22]. The insets in this figure show the pressure distribution outside the forebody, in the flap region with the origin located at  $x = 162.5$  mm.

As it could be expected, an increase in the angle of attack is accompanied by an increase in pressure on the windward side and by a decrease in pressure on the leeward side. The average level of the relative pressure near the stagnation point is about 125, irrespective of the angle of attack. The most pronounced increase in pressure on the flaps is observed on

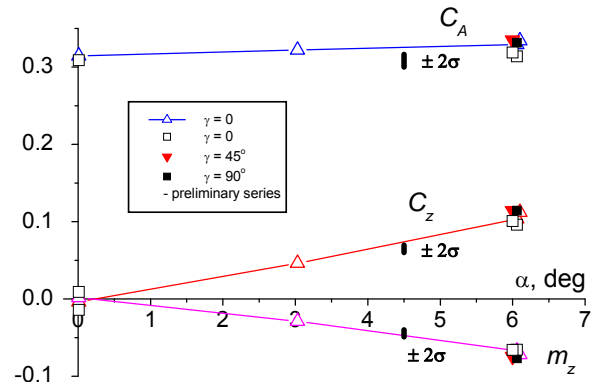
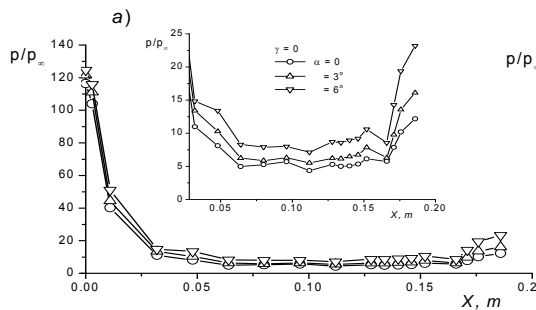


Fig. 15 Aerodynamic characteristics at  $M = 13.8$  and  $Re_1 \sim 1.55 \cdot 10^7$  1/m

a)



b)

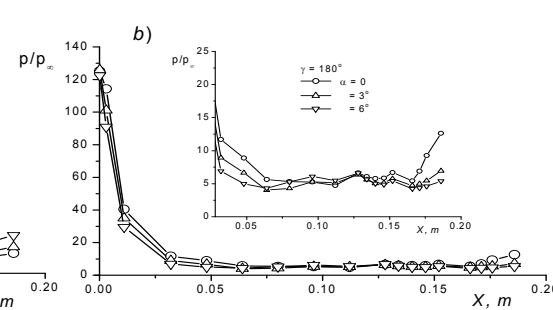


Fig. 16 Distribution of the relative pressure over the windward (a) and leeward (b) surfaces of the model.

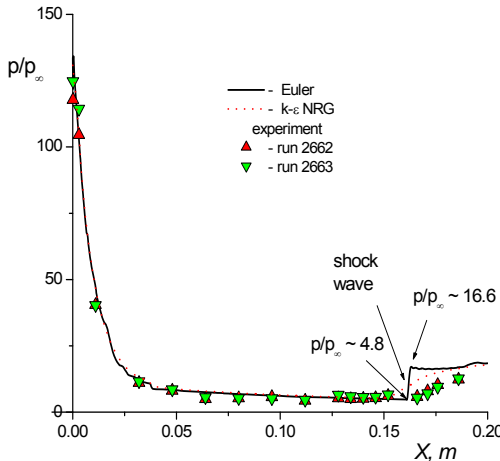


Fig. 17 Calculated and experimental distributions of pressure at zero angle of attack.

the latter pressure level with the simplest estimate of the critical pressure drop  $\bar{p}_{kr} = 1 + 0.5M_1 = 2.4$  for the turbulent boundary layer points to possible separation of the boundary layer caused by shock-wave boundary layer interaction. Subsequent Navier – Stokes calculations confirmed the presence of a separation zone in the flap region. Note also that the pressure distributions outside the separation region in viscous and inviscid calculations almost coincide.

**Heat-flux distribution over the surface.** The rapidly changing test conditions in impulse wind tunnels substantially complicate the problem of visualization of the thermal field on the surface and identification of thermal loads. Therefore, panoramic methods of temperature field visualization are preferable in hypersonic facilities, including shock tubes [23, 24].

To obtain the maximum possible reliable information, the thermal loads are measured by calorimetric heat-flux probes and two panoramic methods based on the use of temperature-sensitive coatings and infrared imaging. By comparing the data obtained by different methods, it is possible to determine the range of their applicability (in terms of the run time and the angle of observation of the examined surface) and, thus, obtain reliable distributions of the thermal loads with a high spatial resolution.

As an example, we show the heat-flux distributions measured in the AT-303 wind tunnel with a contoured nozzle (exit diameter 400 mm) at the Mach number  $M_\infty = 13.89$  and Reynolds number  $Re_L \approx 5.42 \cdot 10^6$ .

A comparison of the results of panoramic measurements obtained by infrared thermography (IRT) with the data obtained by the calorimetric method shows that the accuracy of the panoramic method depends substantially on the time of the experimental process and on the angle of observation of the examined surface. An increase in the model surface temperature in the course of the experiment above the nominal level leads to significant measurement errors. Significant distortions are obtained when the angle of observation differs substantially from the normal direction to the examined surface. Figure 18 shows the distributions of heat fluxes to the model surface, which were measured by the IRT method at different times. These results are compared with discrete measurements by calorimetric gauges. The data measured by these two methods on the main part of the model body in the time interval of 30–40ms are

increasing the angle of attack to six degrees. Unfortunately, the small number of pressure taps on the flap provides no clear picture of the flow around the flaps, including the boundary-layer separation during the interaction of the boundary layer with the shock wave.

The pressure distribution at a zero angle of attack computed by the FLUENT software system based on solving the Euler and Navier – Stokes equations with the  $k-\epsilon$  RNG turbulence model is shown in Fig. 17. In particular, the Euler calculations allowed us to evaluate the flow quantities in front of the flap and the pressure levels on the flap. For the Mach number in front of the flap and for the pressure drop across the shock, the values  $M_1 = 2.8$  and  $p_2 / p_1 \sim 3.5$  were obtained. A comparison of

in good agreement. The error of IRT measurements on the nose part is caused by the excess of temperatures over the nominal range of the IR imager and by significant variations of the observation angles. The scatter of data on the flap is apparently caused by flow unsteadiness in the reattachment region. Based on results of panoramic measurements with a high spatial resolution (in contrast to the discrete method), the sizes of the separation regions formed ahead of the control flaps and near the junction of the increased-size nose part with the body were determined. In contrast to the distribution of parameters in one section of the model (discrete method), panoramic measurements provide much more information about the formation of the thermal load on the model. It is seen that the separation zone formed by interaction of the shock wave generated by the flap with the boundary layer on the model body extends beyond the side edges of the flap. The separation region size which reaches the maximum value in the plane of symmetry of the flap decreases with distance from this plane. The maximum size of the separation region (21÷23) mm agrees well with calorimetric measurements. The maximum levels of temperature are observed near the leading edge of the flap and its side edges.

Unfortunately, because of significant variations of the angle of observation of the nose part of the model, the IRT results do not allow localization of the maximum heat flux region, which was identified in calorimetric measurements.

Figure 19 shouse the Stanton number distributions along the generatrix of the model at  $M_\infty = 14$  and  $\gamma = 0^\circ$ . It is obvious a good agreement results of calorimetric measurements and infrared imaging.

The heat transfer level was estimated in the form of specific heat fluxes. Reliability of results is confirmed by the good agreement of data measured by three methods on the main part of the model body. A laminar flow is formed on the surface of three variants of the EXPERT model under the test conditions considered.

The pressure and heat flux distributions measured on the surface show the presence of the separation region resulting from the interaction between the shock wave generated by the flap, and the boundary layer on the body. Increased roughness of the nose part (a layer of powder of about 20  $\mu\text{m}$ )

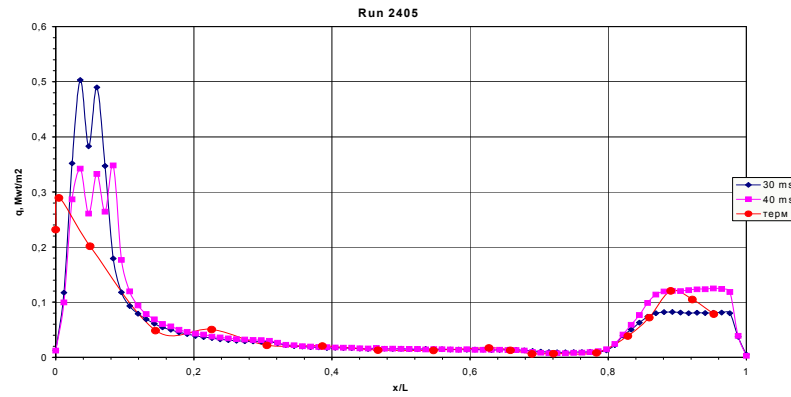


Fig. 18 Heat flux distributions over the surface at  $M_\infty = 14$ . Comparisons of infrared and calorimetric methods.

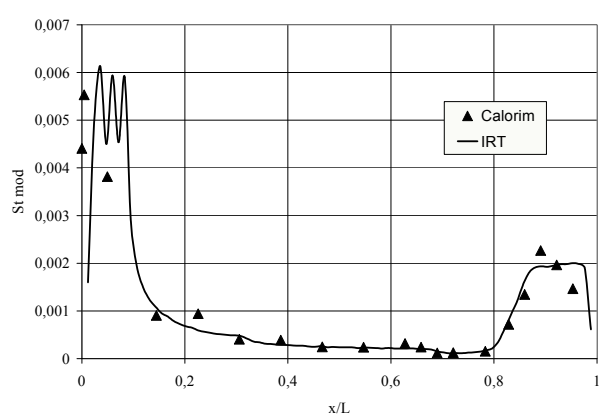


Fig. 19 Stanton number distributions over the surface at  $M_\infty = 14$ ,  $\gamma = 0^\circ$ .

led to a considerable increase in the heat-flux level on the body, reduction of the separation region size ahead of the flap, and thermal load redistribution over the flap surface with a decrease in the maximum heat flux level on it. It can be assumed that the surface roughness changed the flow character in the boundary layer, namely, caused the laminar flow transition to the turbulent one.

This work was sponsored by ISTC within the framework of the projects # 2109, 3151, and 3550.

### **3. Special shock tube for studying magnetohydrodynamic (MHD) methods of flow control**

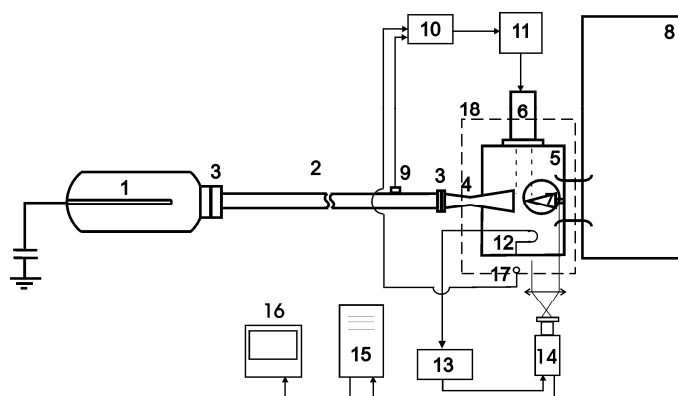


Fig. 20 Sketch of the test rig: 1 – high-pressure chamber, 2 – shock tube, 3 – membrane, 4 – conical nozzle, 5 – test section, 6 – device for external ionization, 7 – model, 8 – receiver, 9 – gauge, 10 – amplifier-generator, 11 – ionizer power supply, 12 – Rogowski coil, 13 – control unit, 14 – CCD camera, 15 – computer, 16 – monitor, 17 – gauge, 18 – magnet-system.

quasistationary parameters during 1÷5ms at  $M = 6, 8, 10$ ,  $P_0 = 5 \div 20$  bar,  $T_0 = 1500 \div 3500$  K, and  $B = (0.0 \div 20)$  T.

Ionization of the flow was performed in the time interval of 50÷100  $\mu$ s, and MHD interaction was studied. Electrodes for initiating local MHD interaction ahead of the model and the model itself (wedge with an angle of 30° between the faces) were located at a distance of 50 mm from the nozzle exit. A specific feature of operation of the impulse gas-dynamic facility based on a shock tube is the

It is well known that the velocity of hypersonic flying vehicles moving at altitudes of 30–50 km reaches 2000 m/s, which allows using the Lorentz force for flow control with actually reachable values of magnetic induction of (2-3)T. A special rig on the basis of a shock tube was developed at ITAM SB RAS for experimental investigations of local MHD processes in the air flow around a wedge and in the case with generation of nonequilibrium conductivity by a pulse electric discharge [25–27]. The test rig (Fig. 20) allows to simulate a hypersonic flow typical of the flight altitude of 30 to 50 km with Mach numbers 6, 8, and 10. This is an impulse-type wind tunnel with

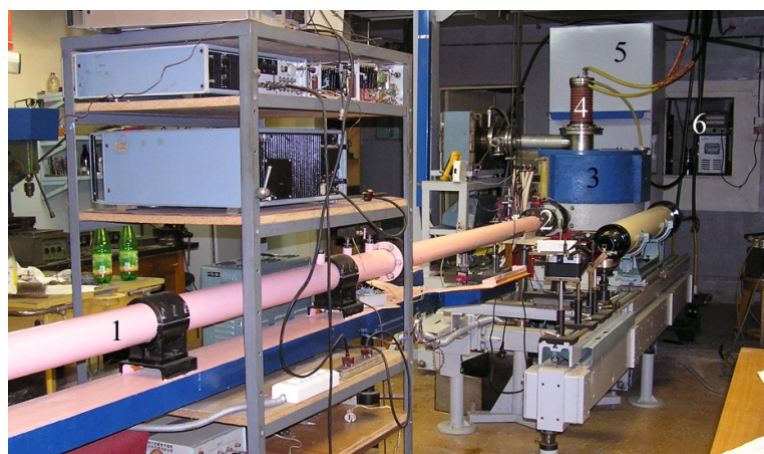


Fig. 21 Photograph of the test rig.

possibility of conducting experiments with almost all cases poured into the low pressure channel of the shock tube. Adiabatic compression of these gases due to deceleration of the shock wave in the settling chamber allows modeling various hypersonic flows. A photograph of the test rig is shown in Fig. 21.

Interaction of the flow with the magnetic field occurs under conditions of nonequilibrium conductivity of the flow, which was generated by an electron beam or by an additional electric discharge on MHD electrodes. The arrangement of experiments is illustrated in Fig. 22.

Tests with an electron beam as a device for ionization were carried out at the Mach number of 8. The static pressure in the flow was about 1.8 Torr, which corresponded to an altitude of about 42 km. The flow velocity was about 2 km per second.

The shock-wave parameters included the pressure and discharge current in the high-pressure chamber, the initial pressure and the shock-wave velocity in the low-pressure chamber, based on the signals of two piezoelectric detectors of pressure.

The parameters in the settling chamber  $P_0$  and  $T_0$  were determined by calculations based on the shock-wave velocity in the high-pressure chamber and the pressure behind the reflected shock wave, which was measured by the piezoelectric detector. The operation parameters of pre-ionizers were determined from the measurements of the pulse discharge current  $I$  and voltage  $U$ . The current was measured by high-frequency current transformers, and the voltage was measured by a voltage divider with inductive output of the signal.

The parameters of MHD interaction were determined from the measurements of the total current in the interaction region and the voltage on the MHD electrodes. In experiments arranged as is shown in Fig. 22, the interaction intensity was determined on the basis of the Stewart number with the use of the measured current in the circuit of the MHD electrodes,

$$S = \frac{IB}{kb\rho V^2} \text{ where } I \text{ is the current, } B \text{ is the magnetic induction, } \rho \text{ is the gas density, } V \text{ is the}$$

flow velocity,  $b$  is the electrode size in the direction perpendicular to the flow, and the coefficient  $k$  takes into account the difference between the effective cross-sectional area of the discharge region and the area of the electrodes, which is equal to the product  $b \cdot l$ . The value of this coefficient is greater than unity. It can be estimated from the size of the luminescent discharge region in the discharge photographs.

The use of an optical schlieren system with the adaptive visualization transparent (AVT) [28] as an optical knife made it possible to stabilize the optical system operation and reduce vibrational noise. Two cameras provided two frames taken at different times, which allowed us to obtain information about the changes in the flow induced by MHD interaction.

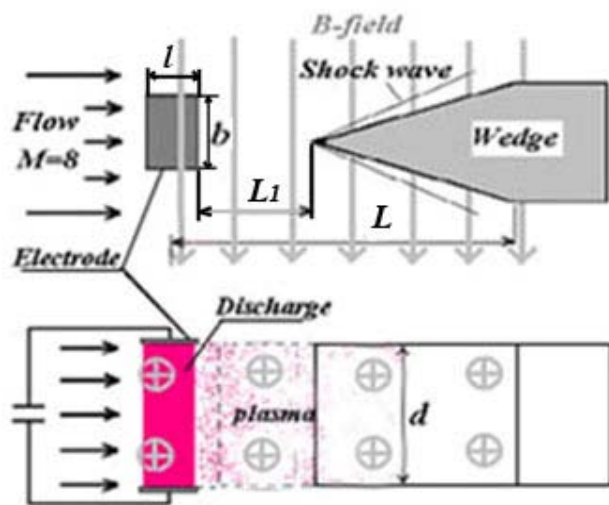


Fig. 22 Schematic of experiments: an E-beam is used as an ionizer. Wedge angle – 30 degrees,  $L=80$  mm,  $L_1=5$  mm,  $d = 50$  mm, electrodes  $b \times l = 15 \times 20$  mm $^2$ .

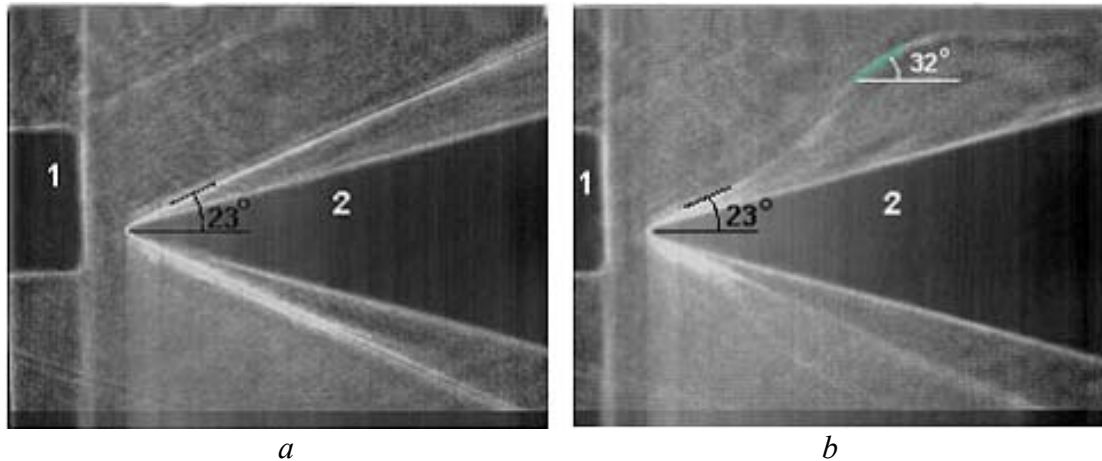


Fig. 23 Photographs of the flow ionized by a pulse discharge, without the magnetic field (a),  $B = 0.0$ , and with the magnetic field (b),  $B = 0.34\text{T}$ . 1 – electrodes, 2 – model (wedge).

Figure 23 shows the schlieren patterns of the flow around a wedge without and with the magnetic field. The static pressure in the flow is  $p_s = 11.6$  torr, the gas density is  $\rho_s = 0.019 \text{ kg/m}^3$ , the temperature is  $T_s = 287 \text{ K}$ , the flow velocity is  $V = 1983 \text{ m/s}$ , and the Mach number is  $M = 5.8$ . The flow parameters are close to the corresponding parameters of the atmosphere at an altitude of 29 km. The time interval between the frames (a) and (b) is 160  $\mu\text{s}$ . Figure 23b shows reconstruction of the shock wave on the wedge after passing through the disturbed flow region.

For the flight time of the flow above the wedge equal to 25  $\mu\text{s}$ , the passage of the MHD-disturbed flow region was registered, and the time of reconstruction of the shock wave on the wedge was estimated (Fig. 23b). The exposure time was 1.2  $\mu\text{s}$ . The frame rate was 330 kHz. A comparison of these photographs allows us to conclude that the slope of the shock wave corresponding to the free-stream Mach number is reconstructed after the MHD-disturbed region passes over the wedge and to determine the relaxation time ( $\sim 3 \mu\text{s}$ ).

Figure 24 shows the shock-wave angle as a function of the MHD interaction parameter  $S$ , with the coefficient  $k = 1.3$ . The angle of the oblique shock was also obtained as a function of the Stewart number for  $M = 8$ , static pressure  $p_{st} = 158 \div 170 \text{ Pa}$  (1.2  $\div$  1.3 mmHg), density  $\rho = 0.0028 \text{ kg/m}^3$ , and velocity  $V \approx 2200 \text{ m/s}$ .

The parameters of MHD interaction were: current  $I = 10 \div 100 \text{ A}$ , voltage on the electrodes  $U_{el} = 190 \div 700 \text{ W}$ , magnetic induction  $B = 0 \div 0.4 \text{ T}$ , flat electrodes,  $b = 15 \text{ mm}$ , and  $k = 1.4$ .

The results of experimental investigations at  $M = 8$  were compared with calculations performed for conditions close to experiments with the use of three-dimensional equations of magnetic gas dynamics under the assumption of small values of the magnetic Reynolds number. Good agreement was reached [29].

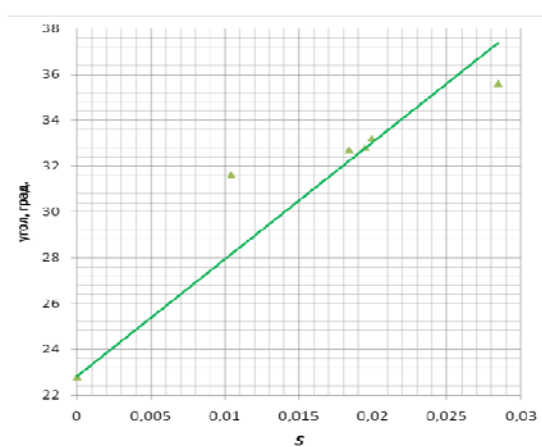


Fig. 24 Shock-wave angle versus the MHD interaction parameter

## References

1. Korolev A.S., Boshenyatov B.V., Druker I.G., Zatoloka V.V. Impulse Wind Tunnels in Aerodynamic Research [in Russian], Nauka, Novosibirsk, 1978.
2. Kharitonov A.M. Techniques and Methods of Aerophysical Experiments Part 1. Wind Tunnels and Gas-Dynamic Facilities [in Russian], NGTU, Novosibirsk, 2005.
3. Zatoloka V.V. Impulse Wind Tunnels [in Russian], Nauka, Novosibirsk, 1986.
4. Dmitriev V.K., Puzyrev L.N., Trushnikov Yu.F., Yaroslavtsev M.I. Hotshot wind tunnel, Authors' Certificate No. 1156462 dated 15.01 1985.
5. Trainneau J.C., Pelissier C., Kharitonov A.M., Fomin V.M., Lapygin V.I., Gorelov V.A. Review of European Facilities for Space Aerodynamics, Technical Report RT 1/06302 DMAE- May 2003.
6. Goonko Yu.P., Kharitonov A.M., Kudryavtsev A.N., Mazhul I.I., Rakhimov R.D. Euler simulations of the flow over a hypersonic convergent inlet integrated with a forebody compression surface, CD-Rom Proc. of European Congress on Computational Methods in Applied Science and Engineering. Barcelona, 11–14 September, 2000.
7. Chalot F., Rostand P., Perrier P., Goonko Y., Kharitonov A., Latypov A., Mazhul I., Yaroslavtsev M. Validation of global aeropropulsive characteristics of integrated configurations, AIAA Paper No. 98-1624, 1998, 8 pp. (AIAA 8th International Space Planes and Hypersonic Systems, and Technologies Conf., Norfolk, USA, 27-30 April 1998).
8. Adamov N.P., Goonko Y., Kharitonov A., Latypov A., Mazhul I., Yaroslavtsev M. Chalot F., Rostand P., Perrier P. Study on drag-thrust forces of a scramjet model in blowdown and hot-shot wind tunnels, Proc. Int. Conf. on the Methods of Aerophysical Research, Novosibirsk, Russia, 1998, Part 3, pp.3-9.
9. Goonko Y.P., Kharitonov A.M., Mazhul I.I., Zvegintsev V.I., Nalivaichenko D.G., Investigation of a scramjet model at hypersonic velocities and high Reynolds numbers, AIAA/AAAF paper 2002-5273.
10. Tret'yakov P.K. Pseudoshock combustion regime, Comb., Expl. Shock Waves, 1993, Vol. 29, No. 6, pp. 694-698.
11. Richards B.E., Enkenhus K. R. Hypersonic testing in the VKI Long-Shot free-piston tunnel, AIAA J., Vol. 8, No. 6, 1969.
12. Pinakov V.I., Rychkov V.N., Topchiyan M.E. Possibility of simulating hypersonic flows on high-pressure adiabatic gasdynamic compression setups, J. Appl. Mech. Tech. Phys., 1982, Vol. 23, No. 1, pp. 56-62.
13. Meshcheryakov A.A., Pinakov V.I., Topchiyan M.E. Stress distribution in the wedge-type piston and the shaft of a system for the adiabatic compression of a gas, J. Appl. Mech. Tech. Phys., 1980, Vol. 21, No. 2, pp. 284-288.
14. Topchiyan M.E., Kharitonov A.M. Wind tunnels for hypersonic research (progress, problems, prospects), J. Appl. Mech. Tech. Phys., 1994, Vol. 35, No. 3, pp. 383-395.
15. Kharitonov A.M., Zvegintsev V.I., Fomin V.M., Topchiyan M.E., Meshcerryakov A.A., Pinakov V.I. New-Generation Hypersonic Adiabatic Compression Facilities with Pressure Multipliers, Chapter 22, Advanced Hypersonic Test Facilities, 2002, pp.583-617.
16. Eitelberg G., Kastell D. Hyperboloid flare experiments in the HEG facility, Report No. HT-TR-E-1-201-DLRG, part II, 1995.
17. Kharitonov A.M., Zvegintsev V.I., Brodetsky M.D., Mazhul I.I., Muylaert J.M., Kordulla W., Paulat J.C., Aerodynamic investigation of aerospace vehicles in the new hypersonic wind tunnel AT-303 in ITAM, Proc. 4th Int. Symp. on Atmospheric Re-Entry Vehicles and Systems, March 21-23, 2005, Arcachon, France.

18. Adamov N.P., Kharitonov A.M., Mazhul I.I., Zvegintsev V.I., Paulat J.-C. Total aerogasdynamic characteristics of the ARES aerospace demonstrator, Proc. 3rd European Conf. for Aerospace Sciences 6–9 July 2009.
19. Walpot L., Ottens H. FESART/EXPERT aerodynamic and aerothermodynamic analysis of the RAV and KHEOPS configurations, Technical report, TOS-MPA/2718/LW, ESTEC, 2002.
20. Ottens H., Walpot L. EXPERT model 4.2, Model description and trajectory analysis. Technical report, TOS-MPA/2749/HO, ESTEC, 2003.
21. Kharitonov A.M., Adamov N.P., Brodetsky M.D., Vaseniov L.G., Mazhul I.I., Zvegintsev V.I., Paulat J.C., Muylaert J.M., Kordulla W. Investigation of aerogasdynamics of re-entry vehicles in the new hypersonic wind tunnel at ITAM, Proc. 44th AIAA Aerospace Sciences Meeting and Exhibit, Jan. 9–12, 2006, Reno, Nevada, USA (AIAA Paper No. 2006-0499).
22. Adamov N.P., Brodetsky M.D., Vaseniov L.G., Mazhul I.I., Zvegintsev V.I., Kharitonov A.M., Paulat J.C., Muylaert J.M., Kordulla, W. Aerodynamics of re-entry vehicles at natural Reynolds numbers. Thermophysics and Aeromechanics, 2006, Vol. 13, No.3, pp.341-351.
23. Mosharov V.E., Radchenko V.N. Measurement of heat fluxes fields in hot-shot wind tunnels with the aid of luminescent temperature transducers, Uch. Zap. TsAGI, Vol. XXXVIII, No. 1-2, 2007, pp. 94–101.
24. Zharkova G.M., Kovrzhina V.N., Petrov A.P., Smorodsky B.V., Knauss H., Roediger T., Wagner S., Kraemer E. Comparative heat transfer studies at hypersonic conditions by means of three measurement techniques. Part I: Measurement techniques, experimental setup and preceding investigations, Proc. Int. Conf. on the Methods of Aerophysical Research (ICMAR) Pt. I. Novosibirsk, 2007, pp. 221–228.
25. Kovrzhina V.N., Kharitonov A.M., Petrov A.P., Shpak S.I., Zharkova G.M., Zvegintsev V.I. The study of hypersonic heat transfer by liquid crystals thermography, Proc. 6th European Symp. on Aerothermodynamics for Space Vehicles, EUCASS, 3–6 November, 2008, Versailles, France.
26. Fomin V.M., Fomichev V.P., Korotaeva T.A., Maslov A.A., Pavlov A.A., Pavlov Al.A., Pravdin S.S., Shashkin A.P., Yakovlev V.I., Malmuth N.D., Smereczniak P., Silkey J.S. Initiation of nonequilibrium conductivity of a hypersonic flow and MHD-interaction, AIAA 2007-1376, 45th AIAA Aerospace Sciences Meeting and Exhibit, Reno, Nevada, 2007.
27. Korotaeva T.A., Pavlov A.A., Pravdin S.S., Fomichev V.P., Shashkin A.P. MHD-effect on location of a bow shock generated by a wedge in a supersonic flow, Proc. Int. Conf. on the Methods of Aerophysical Research (ICMAR), Novosibirsk, 2008, 10 p. CD-ROM.
28. Pavlov A.A., Pavlov Al.A., Golubev M .P. and others, Schlieren device with an adaptive visualization transparent AVT for investigation of flow disturbances creation by optical pulse discharge in gases, Proc. IX Int. Conf. OMIP-2007, M., MEI, pp.174-177.
29. Fomichev V.P., Korotaeva T.A., Shashkin A.P., Yadrenkin M.A.. Investigation of the MHD-interaction in a supersonic flow, Proc. 17th Int. Conf. on MHD Energy Conversion, Shonan Village Center, Kanagawa, Japan, 14–17 September 2009, 13 p.